Eur. Phys. J. D **13**, 11–20 (2001)

THE EUROPEAN PHYSICAL JOURNAL D

EDP Sciences

Spectroscopic studies on Yb^+ ions in liquid helium

Y. Moriwaki[a] and N. Morita

Department of Molecular Structure, Institute for Molecular Science, Myodaiji, Okazaki 444-8585, Japan

Received 27 December 1999 and Received in final form 31 July 2000

Abstract. An emission spectrum of the $4f^{14}\,6s\,^2\mathrm{S}_{1/2}$–$6p\,^2\mathrm{P}_{1/2}$ (D1) transition and excitation spectra of the $4f^{14}\,6s\,^2\mathrm{S}_{1/2}$–$6p\,^2\mathrm{P}_J$ (J=1/2 (D1) and 3/2 (D2)) transitions of Yb^+ ions in liquid helium have been observed by means of a laser-induced fluorescence method. It has been found that all these spectra are blue-shifted from the ones in the free space, and also that the D2 excitation spectrum has double peaks. To understand these spectra, theoretical calculations have also been carried out based on a vibrating bubble model, in which the bubble surface is assumed to vibrate in the spherical (breathing), dipolar and quadrupolar modes. As a result, it has been found that the blue shifts are well understood with this bubble model, and also that the dynamic Jahn-Teller effect due to the quadrupole vibration of the bubble plays an important role for the double-peaked profile of the D2 excitation spectrum.

PACS. 32.30.Jc Visible and ultraviolet spectra – 36.40.Mr Spectroscopy and geometrical structure of clusters – 67.40.Yv Impurities and other defects

1 Introduction

In the past decade, studies on impurity atoms in liquid helium have attracted our interest, and many workers have reported spectroscopic studies on diverse atomic species [1,2]. These studies have so far revealed interesting properties of both impurity atoms and liquid helium, such as a bubble-like cavity structure in liquid helium and its vibrational dynamics, and phonon excitation and exciplex formation of impurity atoms [3–9]. On the other hand, impurity ions in liquid helium have also extensively been investigated so far, and their physical properties have been clarified. However, most of these studies are mainly based on the measurement of kinetic properties (such as the mobility) of impurity ions, and there have been only a few spectroscopic investigations; up to the present, only Ba^+ [10], Sr^+ [11] and Hg^+ [12] ions in liquid helium have been studied by spectroscopic methods.

One of the interesting subjects of studies on impurity ions in liquid helium may be the structure of helium atoms around the ions. More than 40 years ago, Atkins has suggested the possibility that He atoms around an ion form a *snowball* [13]; namely, due to the monopole-induced-dipole interaction, an impurity ion attracts its neighboring He atoms so strongly that a high-density permanent cluster (snowball) of He atoms can be formed around the ion. This snowball model well explains the effective mass and radius of a He^+ ion in liquid helium, but is inconsistent with experimental results of mobility measurements on heavy alkali earth ions, such as Ca^+, Sr^+ and Ba^+ [14]. Concerning this result, Cole and Bachman [15] have inferred that, while a bubble is formed around a heavier alkali earth ion, a snowball can be formed around a lighter one. This is because, while He atoms around a heavier alkali earth ion are pushed away farther from the ion because of the larger orbital radius of its valence electron, He atoms around a lighter ion can approach the ion more closely, which results in the stronger monopole-induced-dipole interactions between the ion and He atoms. Recently, from experimental observations of a significant difference in temperature dependences of mobilities between Be^+ and heavier alkali earth ions (Mg^+, Ca^+, Sr^+ and Ba^+), Foerste *et al.* have inferred that snowballs are formed around Be^+ while bubbles are formed around the heavier ions [16].

In this way, although the structure of helium atoms around impurity ions has gradually been understood through mobility measurements, it still has not completely been clarified at present. A spectroscopic study on impurity ions allows us to view the He structure from its inside, and is, therefore, a useful tool complementary to the mobility measurement. For this reason, more extensive spectroscopic studies are desirable for obtaining more information on the He structure and its dynamics.

In the present work, by means of a laser-induced fluorescence method, we have obtained emission and excitation spectra of the $4f^{14}\,6s\ ^2\mathrm{S}_{1/2}$–$6p\,^2\mathrm{P}_{1/2}$ and $4f^{14}\,6s\,^2\mathrm{S}_{1/2}$–$6p\,^2\mathrm{P}_{3/2}$ transitions of Yb^+ ions in liquid helium. Moreover, we have also theoretically calculated these spectra, and have discussed the experimental results in comparison with the theoretical spectra. In this calculation, following the inference by Cole and Bachman [15], we have assumed a bubble model, not a snowball model,

[a] e-mail: moriwaki@ims.ac.jp

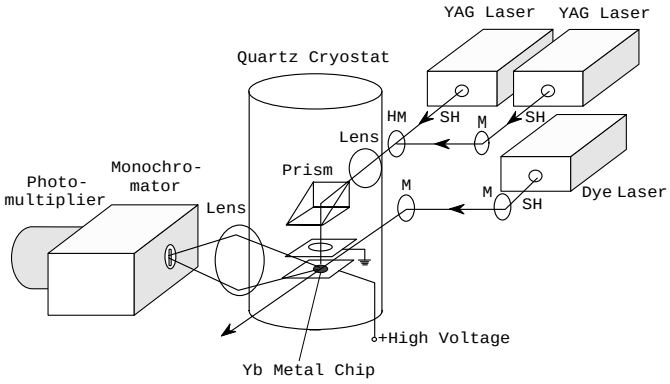

Fig. 1. Experimental setup; M, HM and SH denote a mirror, a half mirror and a second harmonic output, respectively.

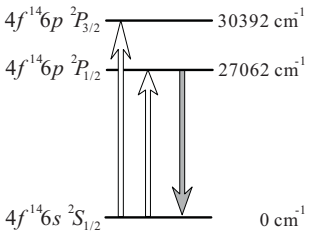

Fig. 2. Schematic diagram of laser excitation, fluorescence and their relevant energy levels of the Yb^+ ion; the energies indicated are those in the free space.

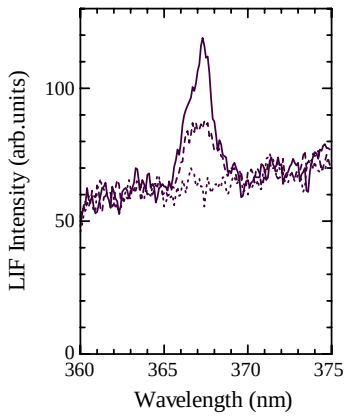

Fig. 3. Examples of emission spectra observed at electric field intensities of 2.8 kV/cm (solid curve), 1.4 kV/cm (dashed curve) and 0 V/cm (dotted curve).

and have also taken into consideration bubble surface vibrations up to the quadrupole modes, similar to the theoretical analysis in a previous study on neutral Rb and Cs atoms in liquid helium [7]. As a result, we have found that spectral properties of our experimental results are in good agreement with the theoretical ones. This result may strongly suggest the validity of the bubble model for Yb^+ ions in liquid helium.

It should be noted that, in the present calculation on the quadrupole vibration of the bubble, all of its five vibration modes have been taken into consideration, although some approximations have been introduced there. In the previous similar calculation mentioned above [7], only two modes out of five are taken into consideration, and it has been considered that this fact results in their smaller theoretical linewidths compared with their experimental ones, as is pointed out by Kanorsky and Weis [17]. Agreements between the experimental and theoretical widths of our excitation spectra are better than those observed in the previous study, and this is probably because of the present improvement in calculation. In this paper, we will describe these experimental and theoretical studies in detail.

2 Experimental

Our spectroscopic observation of Yb^+ ions in liquid helium was performed with an experimental setup shown in Figure 1. Liquid helium was contained in a quartz cryostat at a temperature of about 1.4 K and at the saturation vapor pressure. Ytterbium ions were implanted in the liquid helium by sputtering a small Yb metal chip with two successive second harmonic pulses from two Nd^{3+}:YAG lasers; both lasers were operated at a repetition rate of 10 Hz, the width and energy of each second harmonic pulse were 5 ns and 2 mJ, respectively, and the time interval between the two pulses was 0.1 ms. Both second harmonic beams were collinearly merged with a half mirror and focused on the metal chip with a lens. These two pulses were both necessary for the present observation, because, with only a single pulse, it was impossible to observe any emission that could be assigned to the one from ions. This fact may indicate that, while the first pulse mainly produced neutral and/or ionic clusters, the second pulse efficiently induced the dissociative ionization of the neutral clusters and/or dissociated the ionic clusters. The delay time of 0.1 ms was chosen so as to maximize the emission signal from ions, although no drastic change was seen with varying the delay time around 0.1 ms.

An electrode was placed 7 mm above the metal chip, and an electric field was applied vertically between the electrode and chip. The ions produced by the sputtering were dragged by this field into the observation region a few millimeters above the chip, and were resonantly excited there by a second harmonic pulse of a dye laser 40 μs after the second sputtering pulse; the width and energy of the excitation laser pulse were 5 ns and 0.3 mJ, respectively, and its beam diameter was about 3 mm. Laser-induced fluorescence from the ions in the observation region was introduced into a 25 cm monochromator (with a resolution of 0.2 nm) through a lens and then detected with a photomultiplier.

In the present experiment, the $4f^{14}\,6s\,^2\mathrm{S}_{1/2}$–$6p\,^2\mathrm{P}_{1/2}$ (D1) and $4f^{14}\,6s\,^2\mathrm{S}_{1/2}$–$6p\,^2\mathrm{P}_{3/2}$ (D2) transitions of the Yb^+ ions were excited (the dyes used there were LDS750 and DCM, respectively), as shown in Figure 2. For both excitations, when an electric field was applied (2.8 kV/cm at maximum), an emission spectrum was observed near the D1 transition wavelength (369 nm) of a free Yb^+ ion. As shown in Figure 3, the intensity of this emission decreased with decreasing the electric field strength, and it disappeared at a zero electric field. Judging from such a field-dependence, this spectrum was assigned to an emission spectrum of the Yb^+ ions; it was reasonable to consider that this field-dependence occurred because a higher electric field dragged more ions into the observation region [18]. This spectrum was assigned to the D1 emission of the ions, judging from its frequency. On the other

Table 1. Spectral properties of Yb^+ ions in liquid helium; Δ_s (in cm^{-1}) represents the peak shift from the transition frequency ν_0 (in cm^{-1}) of free Yb^+ ions, and Δ_w (in cm^{-1}) the linewidth in FWHM.

free ion		experimental		theoretical	
transitions	ν_0	Δ_s	Δ_w	Δ_s	Δ_w
$4f^{14}6s\,^2S_{1/2} \rightarrow 4f^{14}6p\,^2P_{3/2}$ (D2)	30 392	556 ±48	386 ± 96	947	340
		1074 ±95	886 ±190	1471	520
$4f^{14}6s\,^2S_{1/2} \rightarrow 4f^{14}6p\,^2P_{1/2}$ (D1)	27 062	644 ±38	386 ± 76	1191	347
$4f^{14}6s\,^2S_{1/2} \leftarrow 4f^{14}6p\,^2P_{1/2}$ (D1)	27 062	132 ±15	146 ± 15	308	55

hand, the D2 emission could not be observed, although we searched it over a wavelength region between 330 and 400 nm, in which, according to our calculation based on an exciplex formation model proposed by Dupont-Roc [19], a broad emission spectrum of the D2 transition was expected to appear. (Details of this calculation will be published elsewhere.) The absence of the D2 emission may probably be due to its weakness, and will be discussed in Section 3.5.

The present measurements were all carried out with the electric field strength fixed at 2.8 kV/cm. As seen in Figure 3, there was a very broad background emission signal around the D1 spectrum, and this signal was independent of the field strength. Therefore, the pure D1 emission spectrum was obtained by subtracting the background signal measured without the electric field from the total spectrum measured with the field. The origin of this background signal was unknown, but it may probably be an emission from neutral Yb atoms or clusters produced by laser sputtering, judging from its field-independence. By monitoring the D1 emission intensity, we also measured excitation spectra of both D1 and D2 transitions. Consequently, we obtained totally three spectra shown in Figure 4. By fitting Gaussian profiles to these spectra, we determined their peak frequencies and widths, which are summarized in Table 1. As seen in Figure 4 and Table 1, these spectra had mainly two characteristics:

(1) all the three spectra were blue-shifted from the ones of free Yb^+ ions,
(2) the D2 excitation spectrum had double peaks.

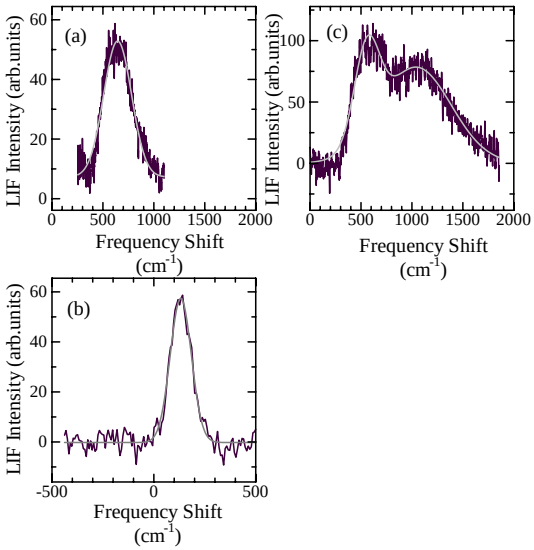

Fig. 4. Experimental spectra of Yb^+ ions in liquid helium; (a) the $4f^{14}\,6s\,^2S_{1/2} \rightarrow 4f^{14}\,6p\,^2P_{1/2}$ (D1) excitation spectrum, (b) the $4f^{14}\,6s\,^2S_{1/2} \leftarrow 4f^{14}\,6p\,^2P_{1/2}$ (D1) emission spectrum, and (c) the $4f^{14}\,6s\,^2S_{1/2} \rightarrow 4f^{14}\,6p\,^2P_{3/2}$ (D2) excitation spectrum. The origin of the abscissa in each figure represents the resonance frequency of each transition in the free space. The gray curve in each figure is a Gaussian profile (the sum of two Gaussian profiles in (c)) fitted to each spectrum.

3 Theoretical calculations and discussions

To understand the above characteristic properties of the D1 and D2 spectra, we have carried out model calculations and obtained the theoretical spectra. In these calculations, as mentioned in Section 1, we have assumed a bubble-like structure for He atoms surrounding an Yb^+ ion, following the inference by Cole and Bachman [15].

Although for the present calculations it is essential to know the form of the interaction potential between an Yb^+ ion and a He atom, there is no useful information on that. Therefore, we have first obtained this potential by an *ab initio* calculation, and then calculated the spectra based on a bubble model.

The most interesting characteristic of the experimental spectra is the double-peaked profile of the D2 excitation spectrum. Such a spectral profile has also been observed in previous studies on Ba^+ [10], Rb and Cs [3] in liquid helium: Reyher *et al.* [10] have pointed out that the double-peaked profile of their Ba^+ spectrum is similar to the one observed in spectroscopic studies on color centers of crystals. Kinoshita *et al.* have successfully analyzed the double-peaked profile of their D2 excitation spectrum of Cs, based on the dynamic Jahn-Teller effect due to quadrupole vibrations of the bubble surface [7]. In view of such previous studies, it is very likely that the present double-peaked profile also arises from a similar dynamic Jahn-Teller effect. Therefore, we have carried out our calculation based on a vibrating bubble model in which distorted vibration modes are taken into consideration.

3.1 Adiabatic potential curves of an Yb^+–He pair

Calculating potential energies of an Yb^+–He pair at each internuclear distance, adiabatic potential curves of this

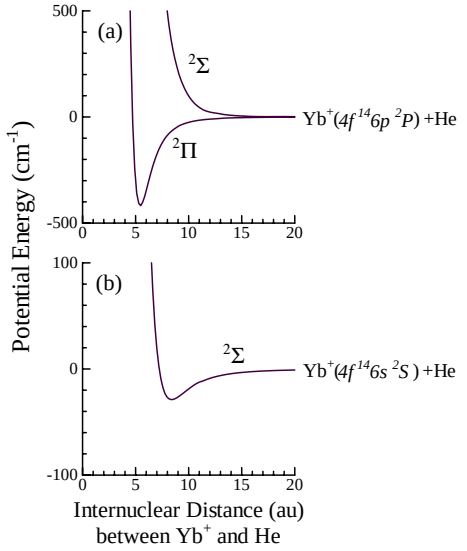

Fig. 5. Adiabatic potential curves of an Yb^+–He pair (a) in the $4f^{14}\,6p\,^2\Pi$ and $^2\Sigma$ states and (b) in the $4f^{14}\,6s\,^2\Sigma$ state.

pair have been obtained. For the Yb^+ ion, we have used 9-valence-electron scalar-relativistic pseudo-potentials with a core polarization and an uncontracted $(9s9p8d6f2g)$ basis set, which have been produced by Dolg *et al.* [20]. As for the He atom, we have used the aug-cc-pVQZ (diffusion function augmented, correlation consistent, polarized valence, double zeta) basis set [21].

Potential energies of the Yb^+–He pair have been obtained by means of the complete-active-space self-consistent field (CASSCF) and multireference configuration-interaction (MRCI) calculations [22,23] in the following way: for the excited states, we have first calculated their electron orbitals in the separate-atom limit ($He(1s^2\,^1S)$ + $Yb^+(4f^{14}\,6p\ ^2P)$ and $He(1s^2\,^1S)$ + $Yb^+(4f^{14}\,5d\ ^2D)$; namely, $4f^{14}\,6p\ ^2\Sigma$, $^2\Pi$ and $4f^{14}\,5d\ ^2\Sigma$, $^2\Pi$, $^2\Delta$), assuming their active space to consist of the $5s$, $5p$, $5d$, $6s$ and $6p$ atomic orbitals of Yb^+ and the $1s$ orbital of He (11 electrons in 14 orbitals). Next, the molecular orbitals for the configuration-interaction calculation have been determined to properly describe the correlation with the separate-atom-limit orbitals, through a state-averaged CASSCF calculation for seven A_1, three B_1, three B_2 and one A_2 states in the C_{2v} symmetry. Finally, using these natural molecular orbitals, we have obtained the potential energies of the Yb^+–He pair by internally-contracted MRCI calculations.

Potential energies of the ground state $(4f^{14}\,6s\,^2\Sigma)$ have also been calculated in a similar way, except that the active space has been assumed to consist of the $5s$, $5p$ and $6s$ orbitals of Yb^+ and the $1s$ orbital of He (11 electrons in 6 orbitals). All these calculations have been performed using a program package MOLPRO [24]. We note that spin-orbit interactions are not included in these calculations. The adiabatic potential curves thus obtained for the ground $4f^{14}\,6s\ ^2\Sigma$ state and excited $4f^{14}\,6p\ ^2\Sigma$, $^2\Pi$ states are shown in Figure 5.

3.2 Vibrating bubble model

The formulation of the vibrating bubble model has already been developed by Hickman *et al.* [25] and Bauer *et al.* [26], and in the present calculations we have followed their formulation, which is in brief as follows: the number density profile of He atoms around an impurity ion is expressed in the form [27]

$$\rho(r) = \begin{cases} \rho_0 \left\{1 - [1 + \alpha(r - r_0)] \exp[-\alpha(r - r_0)]\right\}, & \text{for } r > r_0\ , \\ 0\ , & \text{for } r < r_0\ , \end{cases} \tag{1}$$

where ρ_0 is the number density of helium atoms in the normal region, and r_0 and α are parameters describing the size of the bubble and the slope of the bubble interface, respectively. For a vibrating bubble, r_0 is a function of the solid angle Ω:

$$r_0 = r_e + \sum_{\substack{\lambda=0,1,2,\ldots \\ \mu=0,1,2,\ldots,\lambda \\ \nu=\begin{cases}\pm & (\text{for } \mu \neq 0) \\ + & (\text{for } \mu = 0)\end{cases}}} a_{\lambda\mu\nu} Y'_{\lambda\mu\nu}(\Omega), \tag{2}$$

where

$$Y'_{\lambda\mu+}(\Omega) = \begin{cases} \sqrt{2}\ \mathrm{Re}\ Y_{\lambda\mu}(\Omega), & \text{for } \mu \neq 0, \\ \mathrm{Re}\ Y_{\lambda 0}(\Omega), & \text{for } \mu = 0, \end{cases} \tag{3}$$

$$Y'_{\lambda\mu-}(\Omega) = \sqrt{2}\ \mathrm{Im}\ Y_{\lambda\mu}(\Omega), \qquad \text{for } \mu \neq 0, \tag{4}$$

and $Y_{lm}(\Omega)$ is the spherical harmonic function. The terms with $\lambda = 0$, 1, 2, ... in equation (2) represent the bubble vibrations in the spherical mode (breathing mode), dipole mode, quadrupole mode, and so on, respectively, and $a_{\lambda\mu\nu}$ is the vibration amplitude in each mode.

The Hamiltonian of an Yb^+ ion in liquid helium is given by [28]

$$H = E_l + A_{ls}\mathbf{l}\cdot\mathbf{s} + H_{int} + E_c, \tag{5}$$

where E_l is the atomic energy excluding the spin-orbit coupling, A_{ls} the spin-orbit coupling constant, H_{int} the interaction energy between Yb^+ and surrounding He atoms, and E_c the bubble cavity energy consisting of the surface energy, pressure volume work and volume kinetic energy of the bubble [28]. In the right side of equation (5), while E_l and $A_{ls}\mathbf{l}\cdot\mathbf{s}$ are independent of the bubble vibrations, H_{int} and E_c are functions of the vibration amplitudes $a_{\lambda\mu\nu}$.

In the first-order approximation, the interaction Hamiltonian H_{int} is described by the sum of the potential energies of all Yb^+–He pairs, and is given by [17,29]

$$H^s_{int} = \int \mathrm{d}V \rho(\mathbf{r}) V^s_\Sigma(r), \tag{6}$$

for the $Yb^+(4f^{14}\,6s\,^2S_{1/2})$ bubble and

$$H^p_{\rm int} = \int {\rm d}V \rho(\mathbf{r}) \times \left\{ V^p_\Sigma(r) + \left(\frac{\mathbf{l}\cdot\mathbf{r}}{\hbar r}\right)^2 [V^p_\Pi(r) - V^p_\Sigma(r)] \right\}, \quad (7)$$

for the $Yb^+(4f^{14}\,6p\,^2P_J)$ bubble. Here, $V^l_\Sigma(r)$ and $V^l_\Pi(r)$, in which $l = s$ or p, represent the potential energies of an Yb^+–He pair in its molecular states indicated by the subscripts, and the superscripts s and p indicate the $^2S_{1/2}$ and ^2P_J states of the Yb^+ ion, respectively. These potential energies at each r are given by the adiabatic potential curves calculated in Section 3.1.

Using a basis set $\{|J = 1/2,\, M_J = 1/2\rangle,\, |1/2, -1/2\rangle,\, |3/2, 3/2\rangle,\, |3/2, 1/2\rangle,\, |3/2, -1/2\rangle,\, |3/2, -3/2\rangle\}$, which is a set of angular parts of the ^2P_J $(J = 1/2, 3/2)$ wavefunctions, equation (7) is expressed in the form

$$H^p_{\rm int} = \int {\rm d}V \rho(\mathbf{r}) \times \left\{ \frac{2V^p_\Pi + V^p_\Sigma}{3}\mathbf{E} + \sqrt{\frac{4\pi}{15}}(V^p_\Pi - V^p_\Sigma)\mathbf{A} \right\}, \quad (8)$$

where $\mathbf{E}$ is a unit matrix, and $\mathbf{A}$ is a 6×6 Hermitian matrix. Here, every non-zero element in the matrix $\mathbf{A}$ is given by the second-order spherical harmonic function $Y_{2m}(\Omega)$ times a numerical factor. This is because the operator $[(\mathbf{l}\cdot\mathbf{r})/(\hbar r)]^2$ in equation (7) is quadratic with respect to the direction vector $\mathbf{r}/r$ of a surrounding He atom. (Although zeroth-order functions $Y_{00}(\Omega)$ are also generated from this operator, they are all included only in the diagonal elements in Eq. (8).)

Our calculation procedure to obtain theoretical spectra from the above equations is, in principle, as follows:

(1) first, eigenvalue problems of the Hamiltonian H are solved to obtain adiabatic potential surfaces for both initial and final bubble states, as functions of the vibration amplitudes $a_{\lambda\mu\nu}$;
(2) next, a vibrational wavefunction in the initial bubble state is calculated from its potential surface;
(3) then, the time evolution of this wavefunction on the potential surface of the final bubble state is calculated;
(4) finally, calculating an autocorrelation function of this time evolution, we obtain the spectrum by the Fourier transform of the autocorrelation function.

This procedure is called the "spectral method" [30], which is also used in our previous work on Mg in liquid helium [8].

As mentioned before, non-zero elements of the matrix $\mathbf{A}$ in equation (8) are all proportional to $Y_{2m}(\Omega)$. Therefore, because of the orthogonality of spherical harmonic functions, all non-zero off-diagonal elements of the interaction Hamiltonian $H^p_{\rm int}$ take their largest values when the bubble vibration is in the quadrupole mode described by the $\lambda = 2$ terms in equation (2). This means that the quadrupole vibration is expected to make the largest contribution to spectral properties of the bubble. Based on this fact, we have taken into consideration only three lowest order vibration modes up to the quadrupole mode. However, even in such a simplified case, it is quite difficult to calculate the spectrum by taking into consideration all these three modes simultaneously. Therefore, we have analyzed each of these modes independently, and then obtained the final form of the spectrum by convolution of three spectra obtained from these individual analyses.

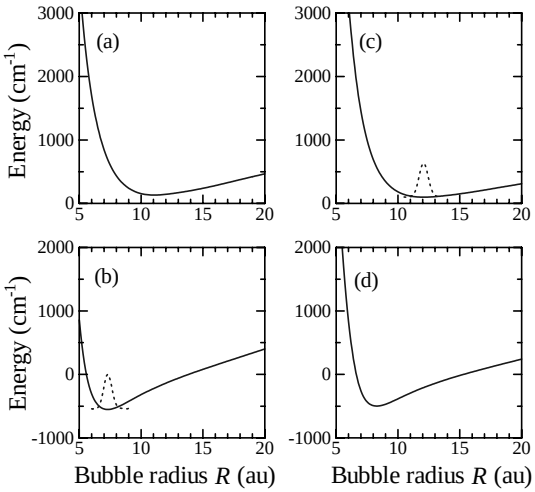

Fig. 6. Total potential energies of spherical bubbles as a function of the bubble radius R; those for the $Yb^+(^2P_J)$ bubble are shown in (a) and (c), and those for the $Yb^+(^2S_{1/2})$ bubble in (b) and (d). In (a) and (b), which are drawn for understanding of the excitation spectra, the bubble parameter α is determined to minimize the total energy of the $Yb^+(^2S_{1/2})$ bubble. The dotted curve in (b) shows the wavefunction for the ground vibrational state of this bubble. In (c) and (d), which are drawn for understanding of the emission spectra, α is determined to minimize the total energy of the $Yb^+(^2P_J)$ bubble. The dotted curve in (c) shows the wavefunction for the ground vibrational state of this bubble.

3.3 Excitation spectra

3.3.1 Excitation spectra due to the breathing vibration

First, we consider the breathing vibration of a spherical bubble. In this case, equation (8) is simplified into the form

$$H^p_{\rm int} = 4\pi \int r^2 {\rm d}r \rho(r) \frac{2V^p_\Pi(r) + V^p_\Sigma(r)}{3}\,. \quad (9)$$

From equations (5, 6, 9), adiabatic potential energy curves for the spherical $Yb^+(^2P_J)$ and $Yb^+(^2S_{1/2})$ bubbles have been calculated as functions of the bubble radius R, as shown in Figures 6a and 6b, respectively. Here, R is defined by the equation $\int_{r_0}^{R} r^2 {\rm d}r\rho(\mathbf{r}) = \int_R^\infty r^2 {\rm d}r(1-\rho(\mathbf{r}))$. Note that, throughout the calculation described in this subsection (Sect. 3.3), the bubble interface parameter α

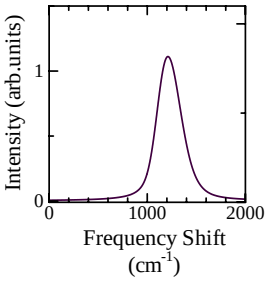

Fig. 7. Excitation spectrum calculated by taking into consideration only the breathing vibration of spherical bubbles. The origin of the abscissa represents the transition frequency of a free Yb^+ ion.

(= 2.7 au^{-1}) is determined to minimize the total energy of the $Yb^+(^2S_{1/2})$ bubble because our purpose here is to obtain excitation spectra from the $^2S_{1/2}$ state.

From the adiabatic potential curve thus obtained, a wavefunction for the ground vibrational state of the Yb^+ ($^2S_{1/2}$) bubble has been calculated by taking into consideration the effective mass $4\pi R^3\rho_0 m_{He}$ for the breathing vibration [31], where m_{He} represents the mass of He. The profile of this wavefunction is also shown in Figure 6b. Since the energy of the first excited vibrational state is calculated to be 17.7 cm^{-1} above the ground state, we can neglect all excited vibrational states at the present temperature of 1.4 K. Therefore, from the wavefunction obtained above and the adiabatic potential curve for the $Yb^+(^2P_J)$ bubble, the excitation spectrum has been calculated by means of the spectral method [30]. The calculated result is shown in Figure 7. As seen in Figure 7, the excitation spectrum is blue-shifted, and this is in qualitative agreement with the D1 and D2 excitation spectra observed in the experiment. However, it does not explain the double-peaked profile of the D2 excitation spectrum.

3.3.2 Excitation spectra due to the dipole vibration

Next, we consider higher vibration modes. For the dipole and quadrupole modes, it is, in principle, necessary to discuss the potential energies and vibrational wavefunctions defined in the three- and five-dimensional $a_{\lambda\mu\nu}$-spaces, respectively; namely, we need to make analyses based on the potential energies $\mathcal{V}^{L_J}(a_{11-}, a_{10+}, a_{11+})$ and wavefunctions $\Psi^{L_J}(a_{11-}, a_{10+}, a_{11+})$ for the dipole mode, and $\mathcal{V}^{L_J}(a_{22-}, a_{21-}, a_{20+}, a_{21+}, a_{22+})$ and $\Psi^{L_J}(a_{22-}, a_{21-}, a_{20+}, a_{21+}, a_{22+})$ for the quadrupole mode. Here, the superscript L_J takes $S_{1/2}$, $P_{1/2}$ and $P_{3/2}$, indicating the $6s\,^2S_{1/2}$, $6p\,^2P_{1/2}$ and $6p\,^2P_{3/2}$ states of Yb^+, respectively.

In general, to solve such multi-dimensional problems requires a huge calculation, and is even unrealistic. For the dipole mode, however, from the analysis of equations (6, 8) we see that the potential energies $\mathcal{V}^{L_J}(a_{11-}, a_{10+}, a_{11+})$ for the relevant three states of Yb^+ are all spherically symmetric in the three-dimensional $a_{1\mu\nu}$-space. This fact is confirmed with Figures 8a and 8b, in which we show potential energy curves $E = \mathcal{V}^{L_J}(a_{11-}, 0, 0)$, $\mathcal{V}^{L_J}(0, a_{10+}, 0)$ and $\mathcal{V}^{L_J}(0, 0, a_{11+})$. (Note that, not only in the calculation of these curves but also in all calculations on the dipole vibration, the amplitude of the breathing vibration is fixed at its minimum potential energy point.) Because of such spherical symmetry of the potential energy, the vibrational wavefunction $\Psi^{S_{1/2}}(a_{11-}, a_{10+}, a_{11+})$ for the ground vibrational state of the $Yb^+(^2S_{1/2})$ bubble is also spherically symmetric. Therefore, this wavefunction is described as a function of the single variable $a \equiv (a_{11-}^2 + a_{10+}^2 + a_{11+}^2)^{1/2}$. We can ignore all excited vibrational states at the present temperature of 1.4 K, since the energy of the first excited vibrational state is calculated to be 27.4 cm^{-1} above the ground state. Similarly, because of the spherical symmetries, potential energies of both $Yb^+(^2P_{1/2})$ and $Yb^+(^2P_{3/2})$ bubbles can also be described as functions of the single variable a.

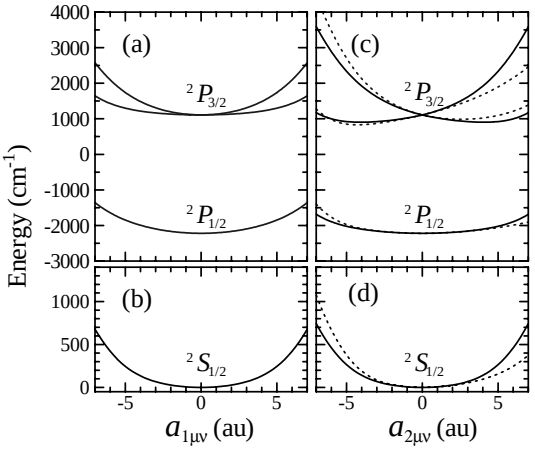

Fig. 8. Adiabatic potential curves for the dipole ((a) and (b)) and quadrupole ((c) and (d)) vibration modes as functions of each amplitude component $a_{\lambda\mu\nu}$ of these modes; in each mode, the upper figure shows the curves for the $Yb^+(^2P_J)$ ($J = 1/2$, 3/2) bubble, and the lower one for the $Yb^+(^2S_{1/2})$ bubble. In (c) and (d) (quadrupole mode), the curves for the a_{20+} component are drawn by dotted curves, and those for the other components, which are identical to each other, are drawn by solid curves. In (a) and (b) (dipole mode), the curves for all $a_{1\mu\nu}$ components are identical to each other.

Due to these facts, the calculation of excitation spectra is much simplified, and the spectra can easily be calculated by means of the spectral method [30]. (Note that vibrational wavefunctions for the dipole mode ($\lambda = 1$) discussed here and for the quadrupole mode ($\lambda = 2$) discussed later are calculated by taking into consideration the effective mass $\rho_0 R^3 m_{He}/(\lambda + 1)$ of the bubble [32, 33].) Excitation spectra thus obtained are shown in Figure 9a. The strongest spectrum in Figure 9a is due to the D1 transition, and the other two spectra are due to the D2 transition. As seen in this figure, there is a separation between the two D2 excitation spectra, but it is very small. This is because off-diagonal elements of the interaction Hamiltonian H_{int}^p are small for dipole distortions, as discussed before.

3.3.3 Excitation spectra due to the quadrupole vibration

For the quadrupole vibration, the potential energy $\mathcal{V}^{L_J}(a_{22-}, a_{21-}, a_{20+}, a_{21+}, a_{22+})$ for any relevant state

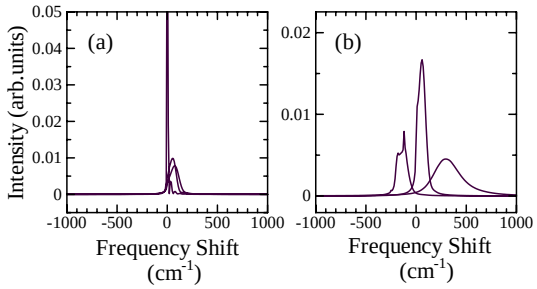

Fig. 9. Excitation spectra calculated (a) when the dipole vibration alone is considered and (b) when the quadrupole vibration alone is considered. In (a), the spectrum with the highest peak is due to the D1 transition, and the other two spectra due to the D2 transition. In (b), the central spectrum is due to the D1 transition, and the others due to the D2 transition. In each figure, the origin of its abscissa represents the resonance frequency of each transition in the free space.

of Yb^+ is not spherically symmetric in the five-dimensional $a_{2\mu\nu}$-space, unlike the case of the dipole vibration discussed above. This is clearly seen in Figures 8c and 8d, in which we show potential energy curves $E = \mathcal{V}^{\mathrm{L}_J}(a_{22-}, 0, 0, 0, 0)$, $\mathcal{V}^{\mathrm{L}_J}(0, a_{21-}, 0, 0, 0)$, $\mathcal{V}^{\mathrm{L}_J}(0, 0, a_{20+}, 0, 0)$, $\mathcal{V}^{\mathrm{L}_J}(0, 0, 0, a_{21+}, 0)$ and $\mathcal{V}^{\mathrm{L}_J}(0, 0, 0, 0, a_{22+})$. (Note that, not only in the calculation of these curves but also in all calculations on the quadrupole vibration, the breathing and dipole vibration amplitudes are fixed at their minimum potential energy points.) As seen in Figures 8c and 8d, for each state of Yb^+, the potential curve $E = \mathcal{V}^{\mathrm{L}_J}(0, 0, a_{20+}, 0, 0)$ is asymmetric with respect to the energy axis at $a_{20+} = 0$, while the other four potential curves are all symmetric and identical to each other. Such an exceptional behavior of the (20+) mode is because of the exceptional form of its mode function $Y'_{20+}(\Omega)$, of which the maximum absolute value is $\sqrt{4/3}$ times larger than those of the other mode functions.

However, for every relevant state of Yb^+, when the vibration amplitudes $a_{2\mu\nu}$ are sufficiently small, there is only a small discrepancy between the potential curve $E = \mathcal{V}^{\mathrm{L}_J}(0, 0, a_{20+}, 0, 0)$ and the other four curves, as seen in Figures 8c and 8d. From this fact, we can infer that, for small vibration amplitudes, the potential energy $\mathcal{V}^{\mathrm{L}_J}(a_{22-}, a_{21-}, a_{20+}, a_{21+}, a_{22+})$ for every Yb^+ state is almost spherically symmetric in the five-dimensional space. This inference allows us to expect that the wavefunction $\Psi^{\mathrm{S}_{1/2}}(a_{22-}, a_{21-}, a_{20+}, a_{21+}, a_{22+})$ for the ground vibrational state of the $Yb^+(^2\mathrm{S}_{1/2})$ bubble is also almost spherically symmetric as long as it is confined within a small amplitude region. However, there is no definite proof for such confinement of the wavefunction; and yet, it is quite difficult to examine such a symmetry property of the wavefunction in the entire five-dimensional space. Therefore, we have examined it by calculating the wavefunction as a function of every two amplitudes out of five; namely, $\Psi^{\mathrm{S}_{1/2}}(a_{22-}, a_{21-}, 0, 0, 0)$, $\Psi^{\mathrm{S}_{1/2}}(a_{22-}, 0, a_{20+}, 0, 0)$, $\Psi^{\mathrm{S}_{1/2}}(a_{22-}, 0, 0, a_{21+}, 0)$, ..., $\Psi^{\mathrm{S}_{1/2}}(0, 0, 0, a_{21+}, a_{22+})$ have been calculated and examined. Consequently, we have found that all these two-variable wavefunctions are nearly identical to each other and almost axially symmetric in the respective two-dimensional spaces, their asymmetries being within 2 percents. From this fact, we can infer that the true wavefunction $\Psi^{\mathrm{S}_{1/2}}(a_{22-}, a_{21-}, a_{20+}, a_{21+}, a_{22+})$ is almost spherically symmetric in the five-dimensional space and described, to a good approximation, as a function of the single variable $a \equiv (a_{22-}^2 + a_{21-}^2 + a_{20+}^2 + a_{21+}^2 + a_{22+}^2)^{1/2}$. Based on this inference, by averaging those two-variable wavefunctions, we have determined the spherically symmetric wavefunction $\Psi^{\mathrm{S}_{1/2}}(a)$. Since the energy of the first excited vibrational state is calculated to be 31.5 cm^{-1} above the ground state, we can ignore all excited vibrational states at the present temperature of 1.4 K.

Using the wavefunction $\Psi^{\mathrm{S}_{1/2}}(a)$ thus obtained, we have calculated excitation spectra by means of the spectral method [30]. Here, also for the $Yb^+(^2\mathrm{P}_J)$ bubbles ($J = 1/2$ and $3/2$), their potential energies $\mathcal{V}^{\mathrm{P}_J}(a_{22-}, a_{21-}, a_{20+}, a_{21+}, a_{22+})$ have been assumed to be spherically symmetric and described by the single variable a. The functional form $\mathcal{V}^{\mathrm{P}_J}(a)$ for each of these potential energies has been determined to be identical to $\mathcal{V}^{\mathrm{P}_J}(a, 0, 0, 0, 0)$ (or equivalent $\mathcal{V}^{\mathrm{P}_J}(0, a, 0, 0, 0)$, $\mathcal{V}^{\mathrm{P}_J}(0, 0, 0, a, 0)$ or $\mathcal{V}^{\mathrm{P}_J}(0, 0, 0, 0, a)$). As discussed before, the potential energies thus determined are not very unrealistic for small vibration amplitudes.

Excitation spectra thus calculated are shown in Figure 9b. The central spectrum in Figure 9b is due to the D1 transition, and the other two spectra at the both sides are due to the D2 transition. This figure shows that the quadrupole vibration causes a large splitting of 450 cm^{-1} in the D2 excitation spectrum. This is a manifestation of the dynamic Jahn-Teller effect due to vibrational quadrupole distortions. For quadrupole distortions, off-diagonal elements in the interaction Hamiltonian H_{int}^p given by equation (8) are so large that the $^2\mathrm{P}_{3/2}$ state of the Yb^+ ion is split in proportion to the amplitude $a_{2\mu\nu}$, as seen in Figure 8c. Consequently, even a small amplitude of the quadrupole distortion causes a sizable splitting in the excitation spectrum.

3.3.4 Final forms of the excitation spectra

Finally, by convolutions of the spectra calculated for the breathing, dipole and quadrupole vibration modes, final forms of the excitation spectra have been obtained. These spectra are shown in Figures 10a and 10c, and their widths and peak shifts are listed in Table 1. As is seen in Figure 10c, the double-peaked profile of the D2 excitation spectrum is well reproduced, and, in particular, the separation between the two peaks is in good agreement with that of the experimental spectrum. These facts indicate that the double-peaked profile can be well understood with our theoretical consideration described above. Moreover, as seen in Figures 10a and 10c and Table 1, spectral widths of the D1 and D2 excitation spectra calculated are both in good agreement with the experimental results. These agreements are better than those observed in the

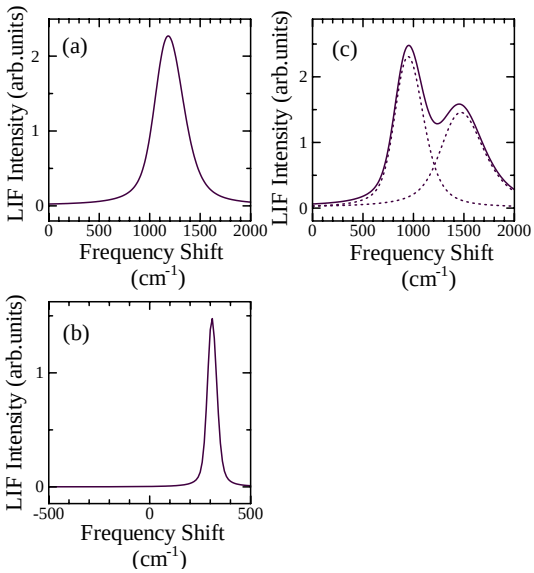

Fig. 10. Calculated spectra; (a) the $6s\,^2\mathrm{S}_{1/2} \rightarrow 6p\,^2\mathrm{P}_{1/2}$ (D1) excitation spectrum, (b) the $6s\,^2\mathrm{S}_{1/2} \leftarrow 6p\,^2\mathrm{P}_{1/2}$ (D1) emission spectrum, and (c) the $6s\,^2\mathrm{S}_{1/2} \rightarrow 6p\,^2\mathrm{P}_{3/2}$ (D2) excitation spectrum. The origin of the abscissa in each figure represents the resonance frequency of each transition in the free space.

previous similar study [7]. This fact is, we believe, because all the five vibration components of the quadrupole mode have been taken into consideration in the present calculation.

On the other hand, blue shifts in both the calculated spectra are larger than the experimental results by roughly 500 cm^{-1}. One of the possible reasons for these discrepancies is that our adiabatic potential for each $\mathrm{Yb}^+(^2\mathrm{S}_{1/2})$–He pair is too deep; due to this large depth, the ground vibrational state of the breathing mode lies as low as -543 cm^{-1}, as seen in Figure 6b. It is quite likely that such too low energy of the initial state causes the too large blue shifts in the excitation spectra.

3.4 Emission spectra

In our experimental observation, while the D1 emission spectrum is observed, no D2 emission is detected with our detection sensitivity. In this subsection, therefore, we will describe the calculation only on the D1 emission spectrum.

For the Yb^+ ion in the $^2\mathrm{P}_{1/2}$ state, spherical bubbles are stable against the distortion, as can be seen from the potential curves in Figures 8a and 8c. Therefore, the D1 emission spectrum can be calculated in the same way as described for the excitation spectra of spherical bubbles in the previous subsection. However, α (= 0.90 au^{-1}) is, in turn, determined to minimize the total energy of the $\mathrm{Yb}^+(^2\mathrm{P}_{1/2})$ bubble. The adiabatic potential curves thus calculated are shown in Figures 6c and 6d. The vibrational wavefunction of the $\mathrm{Yb}^+(^2\mathrm{P}_{1/2})$ bubble is then calculated based on the potential curve shown in Figure 6c. The profile of this wavefunction is also shown in Figure 6c by a dotted curve. The emission spectrum is finally obtained from this wavefunction and the potential curve for the $\mathrm{Yb}^+(^2\mathrm{S}_{1/2})$ bubble by means of the spectral method [30]. The calculated spectrum is shown in Figure 10c, and its spectral properties are listed in Table 1.

As seen in these figure and table, the calculated spectrum shows the same tendencies as seen in the experimental spectrum; namely, both are blue-shifted and have narrow widths compared with the excitation spectra. However, the calculated shift and width are considerably larger and narrower, respectively, than the experimental ones. The too large blue shift may also be due to the too deep potential curve calculated for the $\mathrm{Yb}^+(^2\mathrm{S}_{1/2})$ bubble, similar to the case of the excitation spectra discussed before. On the other hand, the reason for the too narrow width is unknown. This discrepancy might suggest that, also for emission spectra, it is necessary to take into consideration the dipole and quadrupole vibrations in the initial and/or final bubble states. This is interesting future work.

3.5 Deexcitation from the $^2\mathrm{P}_{3/2}$ state

The absence of the D2 emission suggests the presence of fast deexcitation processes from the $^2\mathrm{P}_{3/2}$ state. In this subsection, therefore, we will finally discuss these processes.

Rate equations for the $6p\,^2\mathrm{P}_J$ fine structure levels in the presence of D2 excitation are given by

$$\dot{n}_2 = \Gamma_2 - (k_{21} + A_2 + q_2)n_2 + k_{12}n_1 \,, \tag{10}$$

$$\dot{n}_1 = -(k_{12} + A_1 + q_1)n_1 + k_{21}n_2 \,, \tag{11}$$

where the subscripts 1 and 2 indicate the $^2\mathrm{P}_{1/2}$ and $^2\mathrm{P}_{3/2}$ states, respectively, k_{ij} represents the rate of population transfer from state i to j, and n_i, Γ_i, A_i and q_i represent the population, excitation rate, radiative decay rate and quenching rate of state i, respectively. Rate equations in the presence of D1 excitation are given by similar equations, except that the subscripts 1 and 2 are exchanged. The present temperature (1.4 K) is much lower than the fine-structure splitting (3330 cm^{-1}), so that $k_{12} \ll k_{21}, A_1$ and A_2. From these facts and rate equations, we obtain the following relation at the thermal equilibrium:

$$\frac{k_{21}}{A_2} = \frac{1 + q_2/A_2}{(\Gamma_2/\Gamma_1)(I_1/I_2) - 1} \,, \tag{12}$$

where I_1 and I_2 represent the peak intensities of the D1 emission in the presence of the D1 and D2 excitations, respectively. In our experiment, we can roughly estimate that $(\Gamma_2/\Gamma_1)(I_1/I_2) \sim 2$, so that we obtain the relation $k_{21} > A_2 = 1.6 \times 10^8$ s^{-1} from equation (12). This result means that there is a fast deexcitation process from $^2\mathrm{P}_{3/2}$ to $^2\mathrm{P}_{1/2}$, which competes with or predominates over the radiative decay process of the $^2\mathrm{P}_{3/2}$ state. It is likely that this is one of the reasons for the missing D2 emission.

Here we should note that the D2 emission of Ba^+ has clearly been observed in a similar experiment by Reyher *et al.* [10]. This is in sharp contrast to the present

result, considering that the size of the fine structure splitting in the $6p\,^2P_J$ state does not significantly differ between Ba^+ and Yb^+. In the case of Yb^+, however, there are some $4f$-electron-excited states, such as $4f^{13}(^2F_{7/2})5d6s(^3D)^3[3/2]_{3/2}$ and $^3[11/2]_{9/2}$, near the $4f^{14}\,6p\,^2P_J$ states, unlike the case of Ba^+. Therefore, in addition to the fast deexcitation from $^2P_{3/2}$ to $^2P_{1/2}$, there can also be fast quenching processes from $^2P_{3/2}$ to those nearby states. It is quite likely that this fact causes the crucial difference in the intensity of the D2 emission between Yb^+ and Ba^+.

It is interesting to compare the above estimation on k_{21} with the rate of fine-structure mixing collisions in the gas phase. Although there are no experimental data on such a collision between Yb^+ and He in the gas phase, we can roughly estimate its cross-section from an empirical rule shown by Knoop *et al.* [34]; they have shown that the fine-structure mixing rates of alkali metal atoms (Na to Cs) and alkali earth ions (Mg^+ and Ca^+) due to collisions with He atoms decrease exponentially with the increase of the fine-structure splittings. This empirical rule is also supported by the Laudau-Zener theory. Following this rule, the mixing rate of Yb^+ due to the collision with He is expected to be much smaller than the value of k_{21} ($> 1.6 \times 10^8$ s^{-1}) estimated above. This suggests that the mixing rate in liquid helium is enhanced by some particular mechanism, such as many-body effects and collective motions of helium atoms. It is likely that one of such mechanisms is the quadrupole vibration of the helium bubble. As is seen from equation (8), the mixing between the fine-structure levels arises from the off-diagonal elements of the interaction Hamiltonian $H^p_{\rm int}$. As discussed before, these off-diagonal elements are largest when the bubble is distorted in the quadrupole mode. This fact suggests that the quadrupole vibration of the bubble plays an important role for the strong fine-structure mixing in the $Yb^+(^2P_J)$ bubble.

4 Conclusion

In this study we have, for the first time, experimentally observed emission and excitation spectra of Yb^+ ions in liquid helium. Measuring the $4f^{14}\,6s\,^2S_{1/2} \leftarrow 6p\,^2P_{1/2}$ (D1) emission spectrum and the $4f^{14}\,6s\,^2S_{1/2} \rightarrow 6p\,^2P_J$ ($J = 1/2$ (D1) and 3/2 (D2)) excitation spectra, we have found that all these spectra are blue-shifted from the ones of free ions, and also that the D2 excitation spectrum has a double-peaked profile. Using a Yb^+–He pair potential obtained by our *ab initio* calculation, we have also carried out theoretical calculations based on a vibrating bubble model, in which the bubble surface is assumed to vibrate in the breathing, dipolar and quadrupolar modes. From the qualitative agreements between the experimental and theoretical spectra, it has been found that the Yb^+ ion forms a vibrating bubble cavity in liquid helium, and it has also strongly been suggested that the double-peaked profile of the D2 excitation spectrum is mainly caused by the dynamic Jahn-Teller effect due to quadrupole deformation of the bubble, just like in the case of Ba^+, Rb and Cs in liquid helium. For more quantitative agreements, it is probably necessary to calculate the Yb^+–He pair potential more precisely. Such a calculation is quite difficult to carry out, but is important future work.

A part of the numerical calculations in the present work were carried out at the Computer Center of the Institute for Molecular Science (IMS). We would like to thank Dr. Shinkoh Nanbu of the Computer Center of IMS for his helpful advice on the present calculations. This work was partly supported by a Grant-in-Aid for Scientific Research from the Ministry of Education, Science, Sports and Culture.

References

1. *Ions and Atoms in Superfluid Helium*, edited by H. Günther, G. zu Putlitz, B. Tabbert, Z. Phys. B **98**, No. 3 (1995).
2. B. Tabbert, H. Günther, G. zu Putlitz, J. Low temp. Phys. **109**, 653 (1997).
3. Y. Takahashi, K. Sano, T. Kinoshita, T. Yabuzaki, Phys. Rev. Lett. **71**, 1035 (1993).
4. S.I. Kanorsky, M. Arndt, R. Dziewior, A. Weis, T.W. Hänsch, Phys. Rev. B **50**, 6296 (1994).
5. T. Kinoshita, K. Fukuda, T. Matsuura, T. Yabuzaki, Phys. Rev. A **53**, 4054 (1996).
6. J.L. Persson, Q. Hui, Z.J. Jakubek, M. Nakamura, M. Takami, Phys. Rev. Lett. **76**, 1501 (1996).
7. T. Kinoshita, K. Fukuda, T. Yabuzaki, Phys. Rev. B **54**, 6600 (1996).
8. Y. Moriwaki, N. Morita, Eur. Phys. J. D **5**, 53 (1999).
9. K. Ishikawa, A. Hatakeyama, K. Gosyono-o, S. Wada, Y. Takahashi, T. Yabuzaki, Phys. Rev. B **56**, 780 (1997).
10. H.J. Reyher, H. Bauer, C. Huber, R. Mayer, A. Schäfer, A. Winnacker, Phys. Lett. A **115**, 238 (1986).
11. I. Baumann, M. Foerste, K. Layer, G. zu Putlitz, B. Tabbert, C. Zühlke, J. Low Temp. Phys. **110**, 213 (1998).
12. B. Tabbert, M. Beau, H. Günther, W. Häußler, C. Hönninger, K. Meyer, B. Plagemann, G. zu Pulitz, Z. Phys. B **97**, 425 (1995).
13. K.R. Atkins, Phys. Rev. **116**, 1339 (1959).
14. W.I. Glaberson, W.W. Johnson, J. Low Temp. Phys. **20**, 313 (1975).
15. M.W. Cole, R.A. Bachman, Phys. Rev. B **15**, 1388 (1977).
16. M. Foerste, H. Guenther, O. Riediger, J. Wiebe, G. zu Putlitz, Z. Phys. B **104**, 317 (1997).
17. S.I. Kanorsky, A. Weis, in *Quantum Optics of Confined Systems*, edited by M. Ducloy, D. Bloch (Kluwer Academic Publishers, Netherlands, 1996), p. 367.
18. Because of the lack of data on the mobility of Yb^+ in liquid helium, we cannot exactly estimate the speed of Yb^+ in the electric field. However, for Ba^+, we can estimate it to be about 24 m/s at 2.8 kV/cm and 1.4 K [16]. (The mass ratio between Ba^+ and Yb^+ is not very large, and the bubble sizes for both ions are expected to be comparable because their valence electrons are in the same state ($6s$). Therefore it is likely that the speed of Yb^+ does not much differ from that of Ba^+.) Assuming this speed, the travel distance of the ion is about 1 mm for 40 μs. This distance is comparable to the separation (1–4 mm) between the metal chip and observation region.
19. J. Dupont-Roc, Z. Phys. B **98**, 383 (1995).

20. M. Dolg, private communication; Y. Wang, M. Dolg, Theor. Chem. Acc. **100**, 124 (1998).
21. D.E. Woon, T.H. Dunning Jr, J. Chem. Phys. **100**, 2975 (1994).
22. H.-J. Werner, P.J. Knowles, J. Chem. Phys. **82**, 5053 (1985); P.J. Knowles, H.-J. Werner, Chem. Phys. Lett. **115**, 259 (1985).
23. H.-J. Werner, P.J. Knowles, J. Chem. Phys. **89**, 5803 (1988); P.J. Knowles, H.-J. Werner, Chem. Phys. Lett. **145**, 514 (1988); Theor. Chim. Acta **84**, 95 (1992).
24. MOLPRO is a package of *ab initio* programs written by H.-J. Werner and P.J. Knowles, with contributions from J. Almlöf, R.D. Amos, A. Berning, D.L. Cooper, M.J.O. Deegan, A.J. Dobbyn, F. Eckert, S.T. Elbert, C. Hampel, R. Lindh, A.W. Lloyd, W. Meyer, A. Nicklass, K. Peterson, R. Pitzer, A.J. Stone, P.R. Taylor, M.E. Mura, P. Pulay, M. Schütz, H. Stoll and T. Thorsteinsson.
25. A.P. Hickman, W. Steets, N.F. Lane, Phys. Rev. B **12**, 3705 (1975).
26. H. Bauer, M. Beau, B. Friedl, C. Marchand, K. Miltner, H.J. Reyher, Phys. Lett. A **146**, 134 (1990).
27. J. Jortner, N.R. Kestner, S.A. Rice, M.H. Cohen, J. Chem. Phys. **43**, 2614 (1965).
28. K. Hiroike, N.R. Kestner, S.A. Rice, J. Jortner, J. Chem. Phys. **43**, 2625 (1965).
29. A.D. Wilson, Y. Shimoni, J. Phys. B: At. Mol. Phys. **7**, 1543 (1974).
30. M.D. Feit, J.A. Fleck Jr, A. Steiger, J. Comput. Phys. **47**, 412 (1982).
31. W.B. Fowler, D.L. Dexter, Phys. Rev. **176**, 337 (1968).
32. P.B. Lerner, M.B. Chadwick, I.M. Sokolov, J. Low Temp. Phys. **90**, 319 (1993).
33. A. Bohr, B.R. Mottelson, *Nuclear Structure* (W.A. Benjamin, Inc., Massachusetts, 1975), Vol. II.
34. M. Knoop, M. Vedel, F. Vedel, Phys. Rev. A **52**, 3763 (1995).